A&A 479, 793–803 (2008)
DOI: 10.1051/0004-6361:20077728

Astronomy & Astrophysics

Possible optical detection of a fast, nearby radio pulsar PSR B1133+16⋆

S. V. Zharikov[1], Yu. A. Shibanov[2], R. E. Mennickent[3], and V. N. Komarova[4,5]

[1] Observatorio Astronómico Nacional SPM, Instituto de Astronomía, Universidad Nacional Autónomia de México, Ensenada, BC, México
e-mail: zhar@astrosen.unam.mx
[2] Ioffe Physical Technical Institute, Politekhnicheskaya 26, St. Petersburg 194021, Russia
e-mail: shib@astro.ioffe.ru
[3] Departamento de Fisica, Universidad de Concepcion, Casilla 160-C, Concepcion, Chile
e-mail: rmennick@stars.cfm.udec.cl
[4] Special Astrophysical Observatory, Russian Academy of Science, Nizhnii Arkhyz, Russia, 369167
e-mail: vkom@sao.ru
[5] Isaac Newton Institute of Chile, SAO Branch, Russia

Received 26 April 2007 / Accepted 1 November 2007

ABSTRACT

Aims. We performed deep optical observations of the field of an old, fast-moving radio pulsar PSR B1133+16 in an attempt to detect its optical counterpart and a bow shock nebula.
Methods. The observations were carried out using the direct imaging mode of FORS1 at the ESO VLT/UT1 telescope in the B, R, and H_α bands. We also used archival images of the same field obtained with the VLT in the B band and with the Chandra/ACIS in X-rays.
Results. In the B band we detected a faint ($B = 28\overset{m}{.}1 \pm 0\overset{m}{.}3$) source that may be the optical counterpart of PSR B1133+16, as it is positionally consistent with the radio pulsar and with the X-ray counterpart candidate published earlier. Its upper limit in the R band implies a color index $B - R \lesssim 0\overset{m}{.}5$, which is compatible with the index values for most pulsars identified in the optical range. The derived optical luminosity and its ratio to the X-ray luminosity of the candidate are consistent with expected values derived from a sample of pulsars detected in both spectral domains. No Balmer bow shock was detected, implying a low density of ambient matter around the pulsar. However, in the X-ray and H_α images we found the signature of a trail extending ∼4″−5″ behind the pulsar and coinciding with the direction of its proper motion. If confirmed by deeper studies, this is the first time such a trail has been seen in the optical and X-ray wavelengths.
Conclusions. Further observations at later epochs are necessary to confirm the identification of the pulsar by the candidate's proper motion measurements.

Key words. pulsars: general – pulsars: individual: PSR B1133+16 – stars: neutron

1. Introduction

Until now optical emission has only been detected from ≤1% of ≳1500 known radio pulsars (e.g., Mignani et al. 2005). Even such a small number of optical identifications implies that rotation-powered neutron stars (NSs) can be active in the optical, as well as in the radio range. This follows from the fact that a small group of the optical pulsars contains not only young, ∼1 kyr, and energetic objects like the Crab pulsar (Percival et al. 1993), but also much older pulsars such as ∼3.1 Myr PSR B1929+10 (Pavlov et al. 1996; Mignani et al. 2002), ∼17.4 Myr PSR B0950+08 (Pavlov et al. 1996; Zharikov et al. 2002, 2004), and even the very old ∼1 Gyr recycled millisecond pulsar PSR J0437-4715 (Kargaltsev et al. 2004). The power-law non-thermal spectral component is dominant in the pulsar's optical emission, presumably originating in the magnetospheres of the NSs.

The non-thermal component, which also is frequently observed in a wider spectral range including X-rays, is believed to be powered by the NS rotational energy loss $\dot{E}$, called a spin-down luminosity. The parameter $\eta = L/\dot{E}$, where L is the radiative luminosity, describes the efficiency of the transformation of the rotational energy into the emission. The most striking result of the optical study of ordinary pulsars is that the two old pulsars, PSR B1929+10 and PSR B0950+08, with rather low $\dot{E}$, have almost the same optical efficiency as young and energetic Crab-like objects with much higher spin-down luminosities (Zharikov et al. 2004). At the same time, the efficiencies of middle-aged pulsars are significantly lower. In addition, a strong correlation between the non-thermal optical and X-ray luminosities of pulsars was found, indicating a general origin of the emission in both ranges. (Zharikov et al. 2004, 2006). To confirm these findings it is necessary to increase the number of optically identified pulsars.

An old, ∼5 Myr, nearby pulsar PSR B1133+16 has almost the same parameters as the two old objects mentioned above (see Table 1). It is located at a high galactic latitude, $l = 242°$, $b = 69°$, implying a low interstellar extinction $E(B-V) = 0.04$ (Schlegel et al. 1998). The direct proper motion and annual parallax measurements in the radio range by Brisken et al. (2002) yield a high transverse velocity of 631 ± 30 km s^{-1}

⋆ Based on observations made with ESO telescope at the Paranal Observatory under Program 71.D-0499(A) and with archival ESO VLT data, obtained from the ESO/ST-ECF Science Archive Facility.

Table 1. Parameters of several nearby old pulsars.

Pulsar	Age $\log(\tau)$	Distance* pc	Parallax* mas	μ^*_α mas yr^{-1}	μ^*_δ mas yr^{-1}	$v^*_\perp$ km s^{-1}	$\log(\dot{E})$ ergs s^{-1}	Optical band	Magnitude
PSR B1929+10	6.49	331(10)	3.02(9)	94.8	43	163(5)	33.59	*F342W*	26.8[a]
PSR B1133+16	6.70	350(20)	2.80(16)	–73.95	368.05	631(38)	31.94	–	28.1[d]
PSR B0950+08	7.24	262(5)	3.82(7)	–2.09	29.5	36.6(7)	32.74	*B*	27.07[b]
PSR J0108-1431	8.23	60–130	–	<26	<78	$<50_{130}$	30.75	*B*	>28.6[c]

* Brisken et al. (2002); [a] Pavlov et al. (1996); [b] Zharikov et al. (2002, 2004); [c] Mignani et al. (2003); [d] this paper.

Table 2. Log of the VLT/FORS1 observations of the PSR B1133+16 field during the 2003–2004 periods.

Date UT	UT	Band, exp. number	Exp. s	secz	Seeing arcsec	Sky counts/sec pix	Date UT	UT	Band, exp. number	Exp. s	secz	Seeing arcsec	Sky counts/sec pix
03 Apr. 2003	02:59	*B* 1	1020	1.33	0.95	3.04	-"-	08:03	*B* 12	1020	1.57	0.97	2.53
-"-	03:17	*B* 2	1020	1.31	0.92	3.02	25 Dec. 2003	07:56	*R* 7	485	1.58	0.57	17.38
-"-	03:35	*B* 3	1020	1.31	0.91	2.98	-"-	08:05	*R* 8	485	1.54	0.55	16.80
-"-	03:55	*R* 1	750	1.32	0.77	27.24	-"-	08:15	*B* 13	30	1.50	1.01	-
-"-	04:08	*R* 2	750	1.33	0.71	25.78	19 Jan. 2004	07:24	H_α 1	1550	1.37	0.67	0.65
-"-	04:22	*R* 3	750	1.34	0.71	24.75	-"-	07:51	H_α 2	1550	1.33	0.64	0.67
-"-	04:35	*R* 4	750	1.37	0.73	24.21	25 Jan. 2004	07:08	H_α 3	1550	1.35	0.83	0.71
04 Apr. 2003	03:33	*R* 5	750	1.31	0.91	17.16	-"-	07:35	H_α 4	1550	1.32	0.89	0.74
-"-	03:46	*R* 6	750	1.32	0.84	17.47	26 Jan. 2004	05.46	H_α 5	1550	1.61	0.93	0.59
09 Apr. 2003	02:37	*B* 4	1020	1.32	0.87	5.24	-"-	06:13	H_α 6	1550	1.48	0.83	0.57
-"-	02:55	*B* 5	1020	1.31	0.86	4.14	-"-	06:41	H_α 7	1550	1.40	0.99	0.59
-"-	03:12	*B* 6	1020	1.31	0.95	3.08	-"-	07:08	H_α 8	1550	1.35	1.11	0.57
-"-	03:32	*B* 7	1020	1.32	0.95	2.65	27 Jan. 2004	07:22	H_α 9	1550	1.32	0.88	0.75
-"-	03:49	*B* 8	1020	1.33	0.81	2.62	31 Jan. 2004	07:03	*R* 9	750	1.33	0.56	23.42
-"-	04:08	*B* 9	1020	1.36	0.79	2.70	-"-	07:17	*R* 10	750	1.32	0.66	15.52
24 Dec. 2003	07:28	*B* 10	1020	1.79	0.94	2.56	-"-	07.30	*R* 11	750	1.31	0.89	15.15
-"-	07:46	*B* 11	1020	1.67	0.88	2.52	-"-	07:43	*R* 12	750	1.31	0.83	14.95

and a short distance to the pulsar 350 ± 20 pc. The pulsar is younger than PSR B0950+08, but its spin-down luminosity, 8.8×10^{31} erg s^{-1}, is about an order of magnitude lower than those of PSR B1929+20 and PSR B0950+08. Nevertheless, it is higher than that of the nearby old PSR J0108-1431, whose optical counterpart has been unsuccessfully searched by Mignani et al. (2003). The high transverse velocity is promising for detecting an H_α bow shock nebula expected to be produced by the supersonic motion of the pulsar in the interstellar matter, as has been found around several rapidly moving pulsars and radio-silent NSs (e.g., Gaensler & Slane 2006). Recently, the field of PSR B1133+16 has been observed in X-rays with the Chandra/ACIS and a faint X-ray counterpart candidate was found at a flux level of $(8 \pm 2) \times 10^{-15}$ erg s^{-1}cm^{-2} in 0.5–8 keV range (Kargaltsev et al. 2006). Given this value and using an empirical relation between the optical and X-ray luminosities of pulsars (Zharikov et al. 2004, 2006; see also Zavlin & Pavlov 2004), one can expect to detect the pulsar in the optical range at a sensitivity level of 27–29 mag.

In this paper we present the results of a deep optical imaging of the PSR B1133+16 field taken with the ESO Very Large Telescope (VLT) in B, R_c, and H_α bands to search for the optical counterpart and the bow shock nebula of the pulsar. We also used archival VLT images of the field obtained earlier in the B band and the X-ray data from the Chandra archive. The observations and data reduction are described in Sect. 2. Astrometric and photometric referencing are given in Sect. 3. We present our results in Sect. 4 and discuss them in Sect. 5.

2. Observations and data reduction

The observations were carried out with the FOcal Reducer and low-dispersion Spectrograph (FORS1[1]) at the UT1 (ANTU) unit of the ESO/VLT during several service-mode observational runs from the beginning of April 2003 to the end of January 2004. A standard resolution mode was used with an image scale of ∼0.″2/pixel and field of view (FOV) ∼6.′8 × 6.′8. The total integration time was 12 240 s in B, 8470 s in R_c, and 13950 s in H_α bands. The log of the observations is given in Table 2. To complement our analysis, we retrieved from the ESO archive[2] VLT B-band images of the same field obtained under Program 66.D-0069A of Gallant et al. (2000) in January 2001. These unpublished data were taken with the same telescope unit and instrument in a high resolution mode with an image scale of ∼0.″1/pixel and ∼3.′4 × 3.′4 FOV. The total integration time was about 15 ks. The observational log is given in Table 3.

Generally, all the observations were made under photometric conditions, instrumental magnitude variations of field stars through dataset being insignificant, but the sky background level, seeing, and atmospheric extinction differ. For instance, the individual images in the B and R_c bands for the 2003–2004 period can be subdivided into two distinct groups with a high and low background level (Table 2). The H_α data are more uniform in this respect, but seeing conditions vary from 0.″67 to 1.″11. The 2001 data were obtained under better and less variable seeing

[1] For the instrument details see `www.eso.org/instruments/fors/`
[2] `http:/www.archive.eso.org`

Table 3. The same as in Table 2 but for the 2001 period.

Date UT	UT	Band, exp. number	Exp. s	secz	Seeing arcsec	Sky $\frac{\text{counts}}{\text{sec pix}}$	Date UT	UT	Band, exp. number	Exp. s	secz	Seeing arcsec	Sky $\frac{\text{counts}}{\text{sec pix}}$
18 Jan. 2001	07:41	*B* 1	1000	1.34	0.51	1.63	-"-	07:58	*B* 10	1000	1.33	0.83	0.51
-"-	07:59	*B* 2	1000	1.32	0.57	1.63	-"-	08:16	*B* 11	1000	1.32	0.92	0.53
-"-	08:16	*B* 3	1000	1.31	0.64	1.66	25 Jan. 2001	06:56	*B* 12	1000	1.37	0.58	0.61
-"-	08:38	*B* 4	2	1.32	0.65	6.5	-"-	07:14	*B* 13	1000	1.34	0.63	0.60
-"-	08:39	*B* 5	20	1.33	0.65	6.9	-"-	07:31	*B* 14	1000	1.32	0.67	0.59
19 Jan. 2001	08:09	*B* 6	1000	1.32	0.79	0.96	-"-	07:50	*B* 15	1000	1.31	0.79	0.58
-"-	08:27	*B* 7	1000	1.31	0.85	0.97	-"-	08:10	*B* 16	1000	1.32	0.66	0.57
-"-	08:44	*B* 8	1000	1.31	0.85	1.30	-"-	08:28	*B* 17	1000	1.33	0.66	0.57
22 Jan. 2001	07:41	*B* 9	1000	1.32	0.81	0.51							

conditions, but the sky background level was high for the exposures taken on January 18 and 19, 2001 during moonlight time. (Table 3) The data on January 25, 2001 were obtained under excellent seeing and sky background conditions, but the atmospheric extinction was by ~0.16 mag higher than the standard VLT value, which may be caused by some cirri.

The data reduction including bias subtraction, flat-fielding, removing cosmic ray traces and alignment of each individual image to a reference frame was performed for all the data using standard `IRAF` and `MIDAS` tools. Taking the data non-uniformity into account, we considered different combinations of individual exposures in each band to get co-added images of the best quality, deepness, and spatial resolution. A simple sum of all available images for a given band and period was finally chosen as optimal and subsequently analyzed. Only very short, $\lesssim$30 s, exposures in the *B* band (see Tables 2 and 3) were excluded. As a result, the *FWHM* of a stellar object in the composed images was $\approx 0\farcs75$ and $\approx 1''$ in the *B* band for the 2001 and 2003–2004 periods, respectively. The respective values in the R_c and H_α bands were $\approx 0\farcs85$ and $\approx 1''$. The panoramic view of the pulsar field as seen with the VLT in the *B* band is shown in Fig. 1.

3. Astrometry and photometry

3.1. Astrometry

The *B*-band image obtained by co-adding all *B* band frames taken during the 2003–2004 period was chosen as a base image for our astrometry because its FOV is twice bigger than in the 2001 period. To compute a precise astrometric image solution, the positions of objects selected from the USNO-B1 astrometric catalog[3] were used as a reference. There are about 50 USNO-B1 objects in the FOV in contrast to none from UCAC2. The recent release of the Guide Star Catalog (GSC-II v2.3.2)[4] contains a similar number of stars in this FOV but provides no information on proper motions, and the declared astrometric errors ($0\farcs3$) are higher than nominal $0\farcs2$ uncertainty of USNO-B1. We discarded the reference stars with significant proper motions and catalog-positional uncertainties $\gtrsim 0\farcs4$ along with saturated ones. The pixel coordinates of 30 objects considered to be suitable astrometric reference points were computed making use of the IRAF task *imcenter*. The IRAF tasks *ccmap/cctran* were applied for the astrometric transformation of the image. Formal rms uncertainties of the initial astrometric fit were rather large, $\Delta\mathrm{RA} = 0\farcs287$ and $\Delta\mathrm{Dec} = 0\farcs251$, as compared with the $0\farcs2$ pixel scale of the image. Using standards with the smallest catalog uncertainties and fit residuals significantly improved the fit. For nine reference stars listed in Table 4 and marked in Fig. 1, the formal rms are $\Delta\mathrm{RA} = 0\farcs051$ and $\Delta\mathrm{Dec} = 0\farcs097$, which is smaller than the pixel scale. As can be derived from the Table 4, the local USNO-B1 catalog rms uncertainties of the list in RA and Dec are $\approx 0\farcs045$ and $\approx 0\farcs039$, respectively, which is a factor of four smaller than the nominal catalog uncertainty. To refine the fit, we further removed standards with the largest catalog uncertainties, i.e. the first and the fourth ones from Table 4. This provided much smaller rms, $\Delta\mathrm{RA} = 0\farcs0278$ and $\Delta\mathrm{Dec} = 0\farcs068$, and individual standard residuals $\lesssim 0\farcs09$, which is consistent within 2-σ with the local rms of the catalog and with the positional uncertainties of the standards in the image ($\lesssim 0\farcs05$). We adopted this fit as a final one. It is important that by starting with 13 standards the image transformation became very stable and practically independent of removing other standards with the largest residuals. At these steps coordinate reference points clustered together only within the same image pixel, gradually migrating to some limiting position within this pixel. The same result was obtained using the list of stars with coordinates from GSC-II v2.3.2. Therefore, we are quite confident the derived coordinate reference that is reliable at least at the level of the nominal mean catalog accuracy of $\approx 0\farcs2$. Combining that with the best fit rms, we obtained secure 1-σ uncertainties of our astrometric referencing in the RA and Dec as $0\farcs202$ and $0\farcs211$, respectively. They are comparable with the pixel scale and much smaller than the seeing value.

The co-added 2001 *B*-band image was rebinned by 2×2 pixels to get the same pixel scale as for the 2003–2004 period. All co-added 2001 *B*, R_c, and H_α images were aligned to the base one using a set of suitable unsaturated stars with an accuracy of better than 0.025 pixel size, and the above coordinate reference of the base image was adopted for these images. Formal errors of this referencing are negligible ($\lesssim 0\farcs005$) in comparison with the astrometric referencing uncertainties of the base image. The selection of another summed image, R_c or H_α, as a base does not change the result.

The radio positions of PSR B1133+16 at the epochs of the VLT and Chandra observations (Table 5) were determined using radio measurements of the pulsar proper motion made with the VLA by Brisken et al. 2002. The position errors in Table 5, σ_{RA} and σ_{Dec}, include the errors of the radio position at the reference epoch J2000 (15 mas for both coordinates) and the uncertainties in the pulsar proper motion (0.38 mas and 0.28 mas in RA and Dec, respectively).

Combining the errors of our astrometry and the radio position errors, we derived uncertainties of the pulsar position in our images. Observations in different bands were splinted by

[3] USNO-B1 is currently incorporated into the Naval Observatory Merged Astrometric Dataset (NOMAD), which combines astrometric and photometric information of Hipparcos, Tycho-2, UCAC, Yellow-Blue6, USNO-B, and the 2MASS, `www.nofs.navy.mil/data/fchpix/`

[4] `www-gsss.stsci.edu/Catalogs/GSC/GSC2/GSC2.htm`

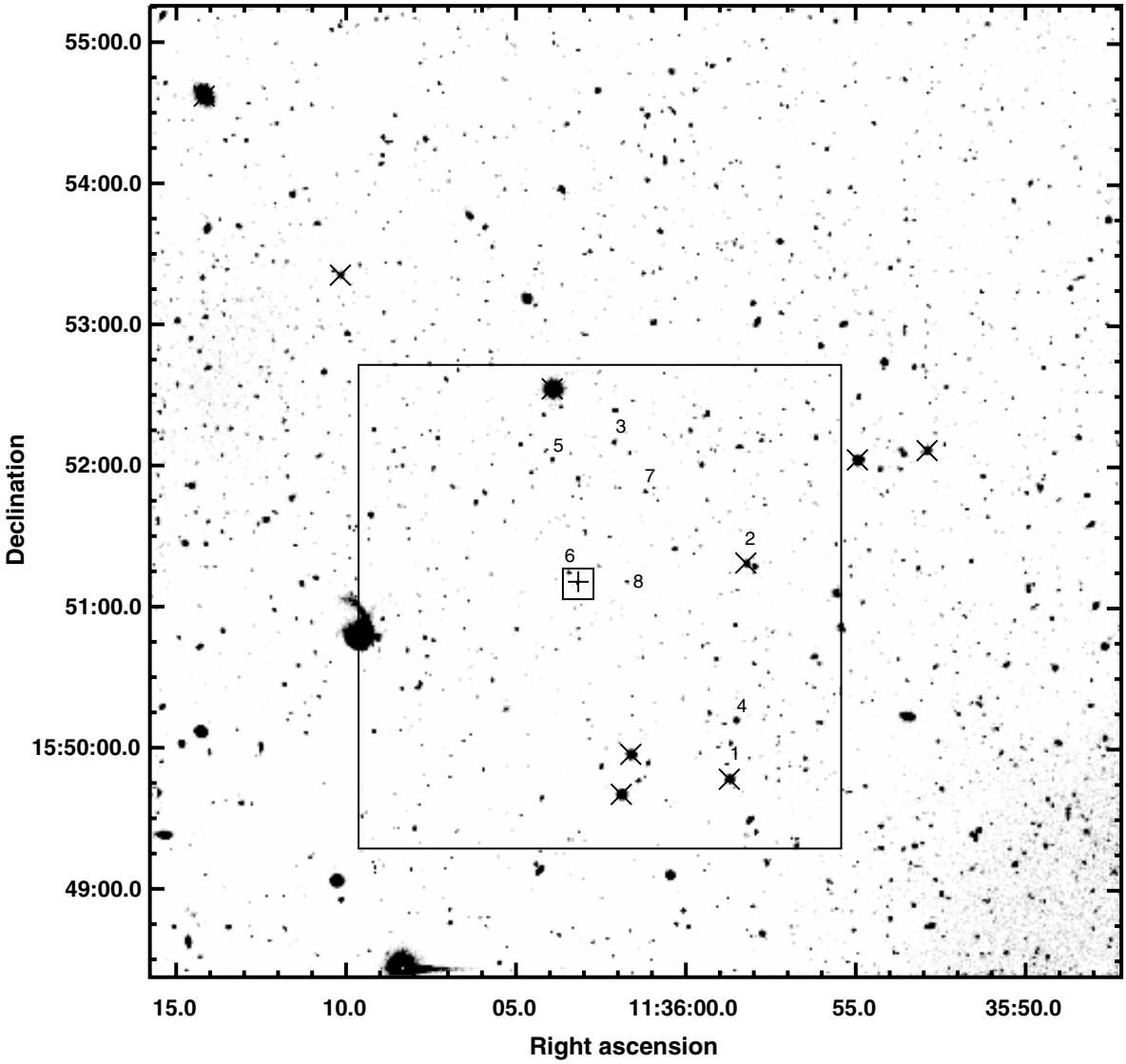

Fig. 1. PSR B1133+16 field as seen in the *B* band with the VLT/FORS1 using a standard resolution mode during the 2003–2004 period. The position of the pulsar is marked by +. The large box marks the FOV of high-resolution mode observations during the 2001 period. The ×-shaped crosses and numbers mark the USNO-B1.0 reference stars from Table 4 and secondary photometric standard stars from Table 7, respectively. The region within a small box is enlarged in Figs. 2 and 4.

Table 4. The list of USNO-B1.0 stars used for astrometrical referencing with coordinates (epoch J2000.0) and their errors.

Name	RA	Dec	σ RA	σ Dec
	hh mm ss	dd mm ss	mas	mas
1058–0205218	11 35 52.8980	+15 52 07.000	192	144
1058–0205222	11 35 54.9493	+15 52 03.040	25	23
1058–0205225	11 35 58.2340	+15 51 19.070	125	239
1058–0205226	11 35 58.7207	+15 49 47.110	307	138
1058–0205233	11 36 01.6207	+15 49 57.610	98	97
1058–0205234	11 36 01.9007	+15 49 40.620	46	47
1058–0205238	11 36 03.9327	+15 52 32.970	34	54
1058–0205246	11 36 10.1713	+15 53 21.120	4	19
1059–0203095	11 36 14.1813	+15 54 37.130	74	109

Table 5. PSR B1133+16 radio coordinates at the epochs of the VLT and Chandra observations.

Epoch	RA	Dec	σ_{RA}	σ_{Dec}
2 450 000+	hh mm ss	dd mm ss	mas	mas
1544.5/2000*	11 36 03.1829	+15 51 09.7257	15	15
1932.5/2001 Jan.	11 36 03.1774	+15 51 10.1189	15	15
2738.5/2003 Apr	11 36 03.1662	+15 51 10.9228	15	15
2997.5/2003 Dec.	11 36 03.1625	+15 51 11.1898	15	15
3029.5/2004 Jan.	11 36 03.1621	+15 51 11.2221	16	15
3424.5/2005 Feb.	11 36 03.1565	+15 51 11.6201	16	16

* Brisken et al. (2002).

different sets on a time basis from a week to 8–9 months, and the pulsar has a large proper motion, particularly along the declination (Table 1) (cf. Tables 2 and 3), therefore one has to account for a systematic uncertainty related to a shift in the pulsar position during this time. It is mostly significant for the *B* and *R* band observations of the 2003–2004 period when the pulsar shifts by ∼0.″197 and ∼0.″229, or by about 1 CCD pixel, from the beginning to the end of the observations. We added these shifts as

Table 6. Expected optical counterpart coordinates at the summed VLT frames.

Frame/ Period	RA hh mm ss	Dec dd mm ss	$3\sigma_{RA}$ arcsec	$3\sigma_{Dec}$ arcsec
B/2001	11 36 03.1774	+15 51 10.1189	0.61	0.63
B/2003	11 36 03.1644	+15 51 11.0563	0.63	1.02
R_c/2003-04	11 36 03.1642	+15 51 11.0719	0.63	1.10
H_α/2004	11 36 03.1621	+15 51 11.221	0.61	0.63

uncertainties squared and calculated the expected optical counterpart coordinates as a simple mean of those at the beginning and the end of the observations for given resulting frames and periods. The results are summarized in Table 6. As seen, despite a rather accurate astrometric referencing of the summed images, the resulting 3σ position uncertainty of the expected optical counterpart can be as large as 1 arcsec in the Dec due to the large proper motion of the pulsar.

3.2. Photometric calibration of the B and R_c images

For precise photometric calibration of all datasets taken in different nights and periods, a two-step approach known as "differential photometry" was applied. At first, absolute magnitudes of a set of relatively bright stars visible in all target frames (so called "secondary standards") were derived accurately. This was done using images of the primary Landolt's standards obtained during the same night chosen as a "reference". In the second step the co-added target images were directly calibrated using the secondary standards. An advantage of this approach is that it is not necessary to consider possible magnitude zero-points and/or extinction variations from night to night since the secondary standards and the target are in the same frames.

The night of 02/03 April 2003 was used as a reference for photometric calibration and, for this night, the zero-points[5] in the Johnson-Cousins B and R_c bands, and color terms establishing the relation between the real B and R_c magnitudes and respective instrumental magnitudes m_B and m_R were derived using 14[6] Landolt's standard stars from Rubin149, PG1047+003, and SA110 fields (Landolt 1992):

$$\begin{aligned} B &= 27.17(3) + m_B - 0.04(2)(m_B - m_R) \\ R &= 27.38(2) + m_R + 0.01(2)(m_B - m_R). \end{aligned} \quad (1)$$

For a star-like object, the instrumental magnitude in jth band is defined as

$$m_j = -2.5\ \log(f^j_{\rm ap}/t_{\rm exp}) - \delta m_j - k_j\ secz\,, \quad (2)$$

where $f^j_{\rm ap}$ is the source flux in counts for a given aperture, $t_{\rm exp}$ the exposure time, k_j the extinction factor, $secz$ is airmass, and δm_j the correction for a finite aperture derived from a point spread function (PSF) of bright stars in the image. The signal-to-noise ratio S/N and magnitude uncertainty Δm are calculated in a standard way as (Newberry 1991)

$$\frac{S}{N} = \frac{f_{\rm ap}}{\sqrt{f_{\rm ap}/g + n_{\rm ap}\sigma^2_{\rm bg}(1 + 1/n_{\rm bg})}} \quad (3)$$

[5] The zero-points were calculated for the flux in ADU/s units. The Paranal Observatory web page lists this night as a photometric one and our zero-points, when converted to electron/s units, are consistent with those provided for this night by the VLT/FORS1 team.

[6] A maximum number of standards per night observed during our program.

Table 7. Secondary standard stars used for photometric referencing.

NN	B mag	R_c mag	H^{AB}_α mag	NN	B mag	R_c mag	H^{AB}_α mag
1	19.91	19.24	19.35	5	22.84	21.40	21.63
2	21.10	20.23	20.37	6	23.04	22.46	22.88
3	22.07	20.47	20.57	7	22.98	20.43	20.35
4	21.27	20.71	21.52	8	24.05	23.32	23.23

Errors are $\pm 0\overset{m}{.}03$ in the B and R_c, and up to $\pm 0\overset{m}{.}05$ in the H_α bands.

$$\Delta m = 1.0856 \left(\frac{S}{N}\right)^{-1}, \quad (4)$$

where $\sigma_{\rm bg}$ is the standard deviation of the background in counts, $n_{\rm ap}$ the number of pixels in the source aperture, g the gain, and $n_{\rm bg}$ the number of pixels in area used for the background measurement. With our seeing conditions, the source aperture with a radius of 3 pixels (at the image scale $\approx 0\overset{''}{.}2$/pixel), for which S/N reaches a maximum, was found to be optimal for stellar objects in all our images. The atmospheric transparency during our reference night was close to a standard value and we used the nominal extinction factors $k_B = 0.25$ and $k_R = 0.08$ provided for the VLT site[7].

The B and R_c magnitudes of the stars chosen as secondary standards were measured at the reference-night images calibrated with the primary standards as described above. The stars are marked by numbers in Fig. 1, and their magnitudes with errors accounting for the zero-point errors shown in brackets of Eq. (1) are listed in Table 7.

Using the secondary standard magnitudes, the resulting zero-points obtained for the images summed over the whole 2003–2004 period are $B = 27.09 \pm 0.03$ and $R_c = 27.37 \pm 0.02$. For the 2001 period the resulting B band zero-point is 26.93 ± 0.03. We also estimated 3σ detection limits of a point-like object in the co-added images. In the B band it is $\sim 28\overset{m}{.}2$ for the both 2001 and 2003–2004 periods, and $\sim 28\overset{m}{.}6$ for the sum of the two periods. It is $\sim 27\overset{m}{.}9$ in the R_c band. There are no significant difference between the B band formal detection limits for both periods. However, an "eye visibility" of a 3σ object is better for the 2001 period. This is due to better seeing conditions and a higher FORS1 resolution setup during this period (see Sect. 2).

Stellar magnitudes M_j can be transformed into absolute fluxes F_j (in erg s^{-1} cm^{-2} Hz^{-1}), whenever necessary, using standard equations

$$\log F_j = -0.4\left(M_j + M^0_j\right), \quad (5)$$

with the zero-points provided by Fukugita (1995): $M^0_B = 48.490$, $M^0_R = 48.800$.

3.3. Flux calibration of the H_α image

Flux calibration in the H_α narrow band ($\lambda = 6563$ Å, $FWHM = 60$ Å) image was done using the spectrophotometric standard HZ44 observed the same nights as the pulsar. The flux F_{H_α} and AB-magnitude $M^{AB}_{H_\alpha}$ of a source in this band are defined as

$$F_{H_\alpha} = C\ \frac{f \times 10^{\,(0.4\ k_{H_\alpha}\ secz)}}{t_{\rm exp}}\ \frac{\rm erg}{\rm cm^2\ s\ Hz} \quad (6)$$

$$M^{AB}_{H_\alpha} = -2.5\ \log(F_{H_\alpha}) - 48.6, \quad (7)$$

[7] http://www.eso.org

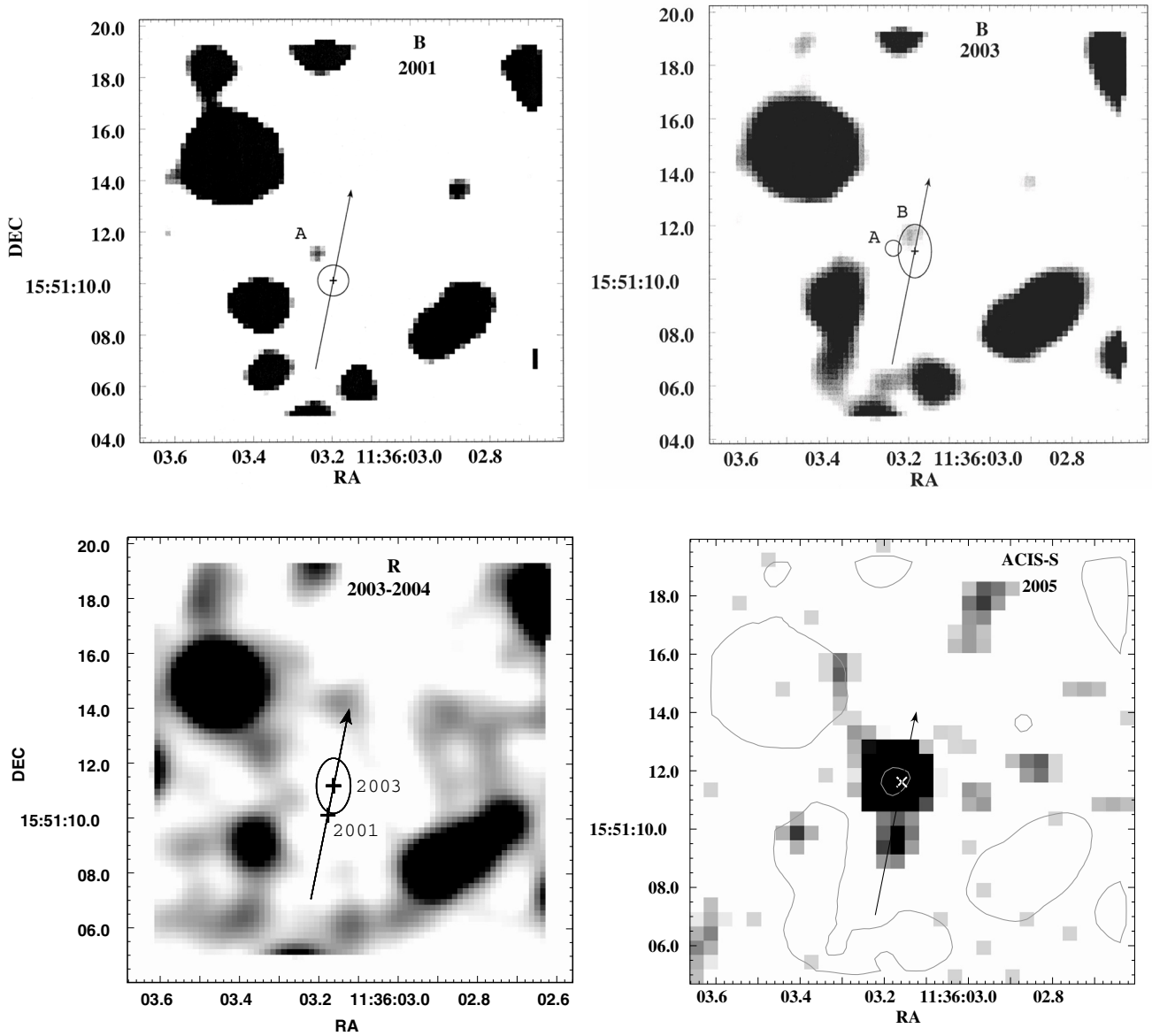

Fig. 2. Fragments of the PSR B1133+16 field images obtained in the optical B and R_c bands with the VLT/FORS1 and in 0.2–10 keV X-ray range with the Chandra/ACIS-S at different epochs, as indicated in the plots. All images are smoothed with ∼1″ Gaussian kernel, and the fragment sizes are ∼14″ × 14″. The + and × mark the expected radio positions of the pulsar at the observing epochs in the optical and X-ray images, respectively. The ellipses show 3σ position uncertainties, and the arrows show the direction of the pulsar proper motion and its path over about 20 yrs. The shift in the pulsar from 2001 to 2003 is indicated in the R_c image. The contour of object A seen in the 2001 B-band image is overlaid on the 2003 B-band image. The contours on the X-ray image are from the 2003 B-band image. Note that object B in the 2003 B-band image nicely fits the position of the candidate X-ray counterpart of the pulsar in the ACIS-S image.

where f is the measured flux of the source in counts and C the calibration constant.

The calibration was performed using the night of 19 January 2004 as a reference. From count-rate variations of stars in the pulsar field with the airmass, we derived a mean atmospheric extinction factor in the H_α band $k_{H_\alpha} = 0.055 \pm 0.017$. Then the calibration constant for this night was derived to be 7.66×10^{-30}. The H_α magnitudes of the secondary standards measured using the reference night image are listed in Table 7. Based on these magnitudes the derived 3σ flux detection limit for a stellar object in the summed H_α image is 1.1×10^{-30} erg cm^{-2} s^{-1} Hz^{-1}, and it is 5.5×10^{-31} erg cm^{-2} s^{-1} Hz^{-1} arcsec^{-2} for a surface brightness of an extended object.

4. Results

4.1. Searching for the pulsar counterpart in the B and R bands

Zoomed fragments of the field containing the pulsar in the B and R bands for the 2001 and 2003–2004 periods are presented in Fig. 2. For comparison we also show the X-ray image of the same fragment obtained with the Chandra/ACIS-S in February 2005[8] where a candidate X-ray pulsar counterpart has been found (Kargaltsev et al. 2006). The expected positions of the

[8] The X-ray data were retrieved from the Chandra archive (Obs. ID 5519, 2005-02-23.18ks exposure, PI G. Garmire.

Table 8. The parameters of the optical objects detected around the expected position of PSR B1133+16.

Object label	RA hh mm ss	Dec dd mm ss	Epoch	Magnitude
A	11 36 03.22 ± 0.04	+15 51 11.16 ± 0.60	2001	$B = 28.0 \pm 0.3$
B	11 36 03.16 ± 0.04	+15 51 11.49 ± 0.60	2003	$B = 28.1 \pm 0.3$, $B - R < 0.5$
C	11 36 03.15 ± 0.04	+15 51 10.86 ± 0.60	2004	$H_{\alpha}^{AB} = 26.3 \pm 0.4$

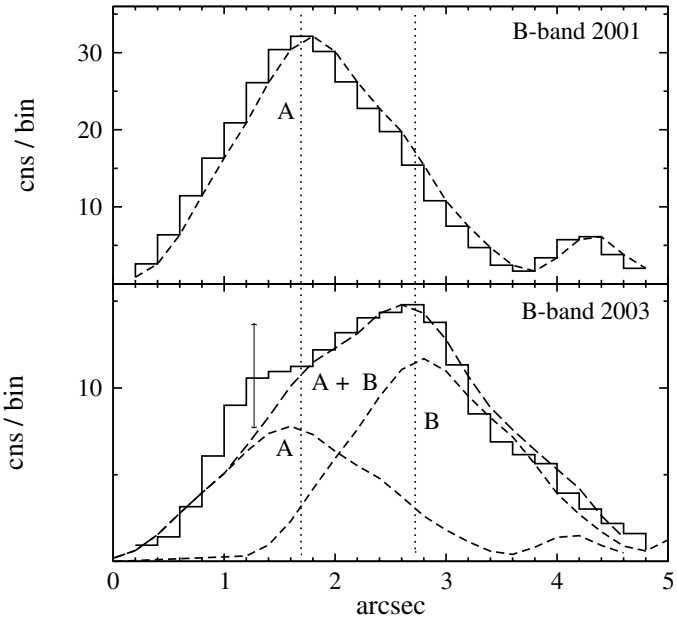

Fig. 3. The observed E-W spatial profiles of the regions containing objects *A* and *B* extracted from the 2001 (top) and 2003 (bottom) *B*-band images of Fig. 2 along the slit with PA of 90° and Dec = +15:51:11.49. The slit length is 4.″6 and its width is 0.″6. The coordinate origin of the horizontal axis corresponds to the eastern edge of the slit with RA = 11:36:03.317. The background was subtracted. Vertical dots mark the positions of *A* and *B* defined from the peaks of the profiles in the top and bottom panels, respectively. The short dashed line in the top panel shows a smoothed *A* profile that is used as a template to fit the *A* + *B* profile in the bottom panel as a sum of the two sources. The resulting fit is shown by the long dashed line, while short dashed lines show the contributions of *A* and *B*.

pulsar for each observing epoch, together with the 3σ position uncertainty ellipses from Tables 5 and 6, are marked with the pulsar proper motion direction.

There are no significant objects within the pulsar position error ellipse in the 2001 *B*-band image. The nearest detected object, marked *A*, is outside the ellipse and lies 1.″1 away from the pulsar 2001 position in a direction not coinciding with the pulsar proper motion. Its *B* magnitude is 28.0 ± 0.3 or only about 3.5σ of the formal detection limit. The outer contour of this object, where it merges with backgrounds, is overlaid on the 2003 *B*-band image. As seen, it only partially overlaps the pulsar error ellipse at the epoch of 2003, although its center is very near to the ellipse border.

At the same time, within the pulsar position uncertainty ellipse in the 2003 *B*-band image, we find another faint object (*B*) with a similar magnitude $B = 28.1 \pm 0.3$. By a good positional coincidence with the expected pulsar coordinates, the object *B* can be considered as a candidate pulsar optical counterpart. The object *A* also can be resolved in this image within its contour of the 2001 epoch (see below). However, it sits in the east wing of the candidate and is not visible in the 2003 *B*-band image of Fig. 2, where the count range is chosen in a such way as to underline the presence of object *B*. The positions and magnitudes of objects *A* and *B* are listed in Table 8.

A thorough inspection of the region containing objects *A* and *B* in the 2001 and 2003 *B*-band images was made with using individual exposures. It confirmed that both objects are real but not artifacts caused by, e.g., a poor cosmic ray removing or flat-fielding. Owing to their closeness and faintness, these objects may represent bright parts of the same unresolved extended background feature. To verify this possibility we considered the changes in spatial profiles of the region containing both objects from one observing epoch to another. Within positional uncertainties, the objects almost have the same declinations, while their right ascensions differ by about one arcsecond. This allows us to compare only 1D E-W spatial profiles at a fixed declination.

In Fig. 3 we present the 1D profiles extracted from the 2001 and 2003 *B*-band images, shown in Fig. 2, along a horizontal slit with PA = 90° and Dec = +15:51:11.49. The slit length and width are 4.″6 and 0.″6, respectively, and the centers of both objects *A* and *B* are within this slit. The coordinate origin of the horizontal axis in Fig. 3 corresponds to the eastern edge of the slit with RA = 11:36:03.317. Only object *A* is seen in the 2001 profile (top panel). The 2003 profile is significantly wider, about twice, and has an asymmetric shape suggesting two sources of different intensities with overlapping profiles (bottom panel). Its peak is shifted towards west and corresponds to the position of object *B*, while object *A* is probably responsible for the "shoulder" in the east profile wing.

The objects are too faint to be resolved reliably as two point-like sources with standard PSF modeling and subtraction tools. To analyze the situation, we applied a simplified approach based on the fact that only a single object *A* is resolved in the 2001 *B*-band image and profile. We used its profile shape as a template of a single source profile to fit the suggested *A* + *B* blend at the 2003 period by a sum of the emissions from two sources, assuming that *B* has the similar profile shape. Within uncertainties, this model is in a good agreement with the 2003 observations if the peak intensity of object *A* is by a factor of 1.5 lower than that of *B*. This corresponds to about a 0.4 mag difference, which is within the uncertainties of the objects' magnitude measurements. The distance between *A* and *B* is about 0.″8–1.″0. This simplified approach supports the interpretation that *A* does not change its position and brightness significantly from the 2001 epoch to 2003, while *B* appears in the 2003 image as an additional source roughly of the same brightness, and by positional coincidence it can be associated with the pulsar. We discuss this and other possibilities of the *A* + *B* interpretation in Sect. 5.

Neither of the objects *A* and *B* are resolved in the *R*-band image, which is obviously shallower due to a shorter integration time (cf. Sect 2). Nevertheless, the absence of a "red" source at the expected pulsar positions allows us to constrain the color index for the candidate detected in the *B* band as $B - R \lesssim 0.5$.

To better compare the 2005 X-ray and the 2003 B-band images we overlaid the contours of the optical image onto the X-ray image. The pixel scale of the ACIS-S image is about 0.″5, which is comparable to the proper motion shift of the pulsar between the 2003 and 2005 epochs, but about three times smaller than the *FWHM* of the ACIS PSF. Within these uncertainties and a nominal ∼1″ Chandra/ACIS pointing accuracy, the contour of the possible optical counterpart, object B, fits the position of the candidate X-ray counterpart nicely, which is the brightest object in the X-ray image. This implies, at least, that we probably see the same object in the optical and X-rays. The position of the X-ray candidate with 0.″2 accuracy coincides with the expected radio position of the pulsar at the epoch of the Chandra observations (Kargaltsev et al. 2006). We also note that counterparts of some other optical objects in the field may be found in the X-ray image and vice versa.

4.2. Possible pulsar tail in H_α and X-rays?

The 2004 H_α-image of the same field and the difference in the H_α and normalized R-band images, where most of the continuum emission is subtracted, are shown in Fig. 4. The contours of the ACIS − S X-ray image, which is also shown here but with a slightly different gray scale than in Fig. 2, are overlaid on the ($H_\alpha - R$)-image and vice versa. As in Fig. 2, all images are smoothed with the Gaussian kernel of about 1″, which roughly corresponds to the seeing of the resulting optical images.

In the H_α image we find a faint point-like source (C), which lies within the pulsar position error ellipse. It is near the detection limit and its star-like H_α^{AB} magnitude is 26.3 ± 0.4 (2.7σ formal detection limit), which corresponds to the flux $F_{H_\alpha} \approx 1.05 \times 10^{-30}$ ergs cm^{-2} s^{-1} Hz^{-1} or 1.5×10^{-6} photon cm^{-2} s^{-1}. The object is not detected in the B and R_c bands, while its possible artifact origin in the narrow band was ruled out after a careful inspection of individual H_α frames.

We do not see any characteristic extended bow shock structure around the pulsar, as is produced, for instance, around another high-velocity pulsar PSR B2224+65, known as the Guitar nebula (Cordes et al. 1993). Instead of that, we see a faint and rather clumpy H_α emission most likely associated with the recombination of a heated ambient matter around background objects of the field. Some of them may have X-ray counterparts. However, there is one faint structure (about 4.5″ length) south of object C. This apparent structure is roughly aligned with the pulsar proper motion direction and located behind its 2003 position. It is better seen in the (H_α-R) image where it merges with object C. There are no signs of the structure in the broad band optical images. At the same time, in the X-ray image, we also see a marginal tail-like structure behind the pulsar counterpart candidate, though of smaller spatial extent. It was not mentioned by Kargaltsev et al. (2006), who only reported on the detection of the X-ray pulsar candidate. If both structures are not background fluctuations, they can be considered as cometary-like pulsar tail candidates.

5. Discussion

In Table 8 we collected the coordinates and magnitudes of the objects detected around the radio positions of the pulsar in each VLT observing epoch. Given that sources B and C are located within 3σ pulsar position error ellipces related to respective observing epochs (cf., Tables 6 and 8), they can be associated with the pulsar. Object B, emitting in a broadband range, can be considered as a candidate pulsar optical counterpart, while C can be a sign of the pulsar interaction with a clumpy ambient ISM seen via the H_α recombination line. Object A is outside of the 3σ-error ellipses for both observing epochs and we qualify it as a background source. If object B detected in the 2003 B-band image is the real counterpart of the pulsar, then why do we not resolve it in the expected place on the 2001 B image?

One of the reasons is the faintness of the object, which is resolved at a level very close to the estimated 3-σ detection limits (see Sect. 3.2). To estimate the probability of detecting an object with $S/N \sim 3$ in our data, we selected almost a homogeneous subset of 2001 B-band images, B12-B17, which provides a maximal number of frames with the same seeing, background, and atmospheric extinction (see Table 3). Then, we selected about 100 faint objects chosen randomly in the sum of these 6 frames and checked that these objects are detected in the each of the individual frames. That was done in two ways. In the first, we used the optimal aperture, with 3 pixel radius, and an object was accepted as detected at an individual image if its magnitude error was less that 0.36, which corresponded to $S/N \approx 3$. In the second way we estimated the object by eye in the images smoothed with the Gaussian kernel. In the first case the probability of detecting an object with $S/N \sim 3$ was 60%–70%. In the second, less formal case, it was about 80%–90%. This means that, if we have two sets of VLT observations in the same band with approximately equal conditions and exposure lengths and detect a faint object with $S/N \sim 3$ in one of them, the probability of losing this object in backgrounds at the second set of observations by pure count statistic is about 10%–40%. Accounting for not quite homogeneous conditions for the 2001 and 2003 periods, a conservative estimate for losing the suggested pulsar optical counterpart at the expected position at the 2001 epoch is about 50%.

In addition, a slightly higher background, e.g., due to the closeness of a nearby bright object east of the pulsar path (cf. Fig. 2) or to a small increase in the interstellar extinction (e.g., by $\Delta E(B-V) \sim 0.04$) for the line of sight towards the 2001 pulsar position can drown the candidate in backgrounds in the 2001 B image.

The pulsar optical brightness variation cannot be excluded also, since it is known to show a pulse nulling phenomenon in the radio range (e.g., Bhat et al. 2007 and references therein). It spends up to 15% of its time in the null state, and shows epochs when its radio flux changes by a factor of two. There are still no direct simultaneous radio and optical observations of pulsars. However, one cannot rule out a link between pulsar activities in these domains since both emissions are governed by complicated NS magnetosperic processes. The 2001 observing period of one week duration is much shorter than the 2003 one spanning 8 months and a chance to meet a comparable flux depression phase that might completely hide the counterpart in the 2001 epoch is higher.

We also cannot exclude the possibility that B is simply a time variable background object or a part of an extended unresolved variable feature that includes A and B as its relatively brighter regions. Another possibility is that A and B represent the same object displaced between 2001 and 2004 epochs by its own proper motion. However, our analysis has shown (Sect. 4.1) that A and B are likely to be two single objects and A does not show any significant variability or proper motion towards the position of B to explain the variability of the latter. We have also found no other variable objects in the pulsar neighborhood at the time base of three years. Possible variability of B can be checked only by further observations. If they will show that B survives and moves

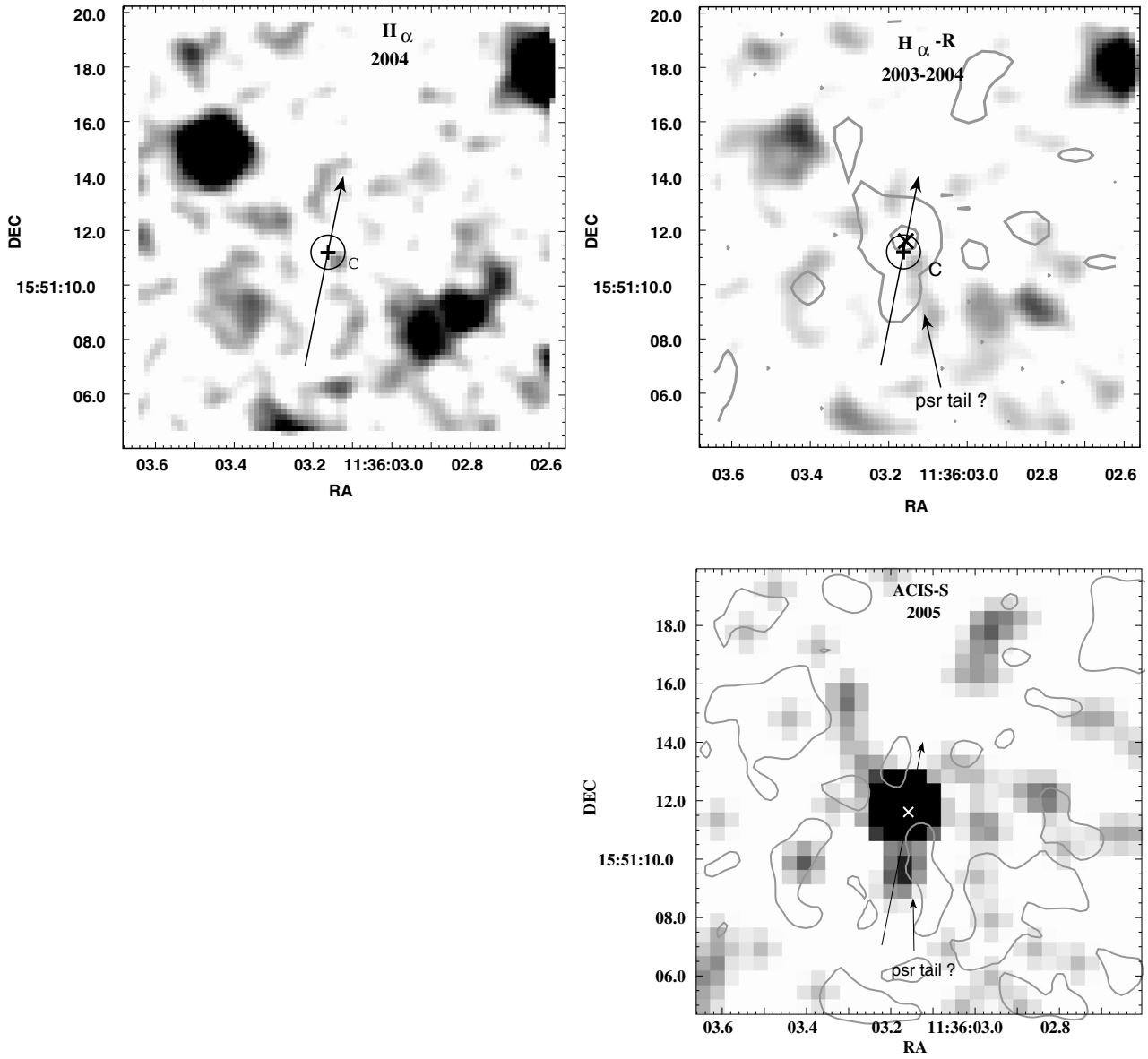

Fig. 4. The same as in Fig. 2 but for the H_α and ($H_\alpha - R$) images, with the contours from the X-ray image overlaid. The X-ray image with the ($H_\alpha - R$) image contours overlaid is also shown for comparison.

consistently with the pulsar this will be a strong proof that we see the real optical couterpart.

A good positional coincidence of B with the candidate X-ray pulsar counterpart suggests that we see the same object in the optical and X-rays. Its color index, $B - R \lesssim 0.5$, is compatible with the indices of Vela pulsar, PSR B0656+14, Geminga, and PSR B0950+08, which all have $B - R$ in a narrow range of 0.46–0.6 (Mignani & Caraveo 2001; Shibanov et al. 2006; Zharikov et al. 2004).

Let us assume that the optical object B and the respective X-ray source are indeed the pulsar PSR B1133+16. The spectral fit of the Chandra/ACIS-S data of the X-ray counterpart candidate by an absorbed power law (Kargaltsev et al. 2006) yields the non-thermal X-ray luminosity of the pulsar $L_X = 5.01(+4.30/-2.41) \times 10^{28}$ in the 2–10 keV range at the distance of 357 pc, or $\log L_X = 28.70(28)$. The corresponding X-ray efficiency is $\log \eta_X = -3.24(28)$, which is not exceptional and lies near the efficiency range of the two other old pulsars, PSR B1929+10 and PSR B0950+08, detected in the optical and X-rays (Zharikov et al. 2004, 2006).

Using η_X and the empirical relation between the non-thermal optical and X-ray efficiencies of ordinary pulsars reported by Zharikov et al. (2004, 2006), we would expect to find the PSR B1133+16 optical counterpart with a magnitude in a range of about 29–30 and with the optical efficiency $\log \eta_{Opt} \approx -6.2$. The proposed candidate is a magnitude brighter and the respective optical luminosity and efficiency, $\log L_B = 26.76(17)$ and $\log \eta_{Opt} = -5.18(17)$, are also about one order of magnitude higher than is expected from the reported relation. However, this may simply reflect inaccuracies in the empirical relation, which is based on a very limited sample of the optically detected pulsars.

To study how this discrepancy can modify the relation and the evolution tendencies considered by Zharikov et al. (2004, 2006), we included the proposed candidate in the sample. The results are shown in Figs. 5 and 6. As seen (Fig. 5), our candidate

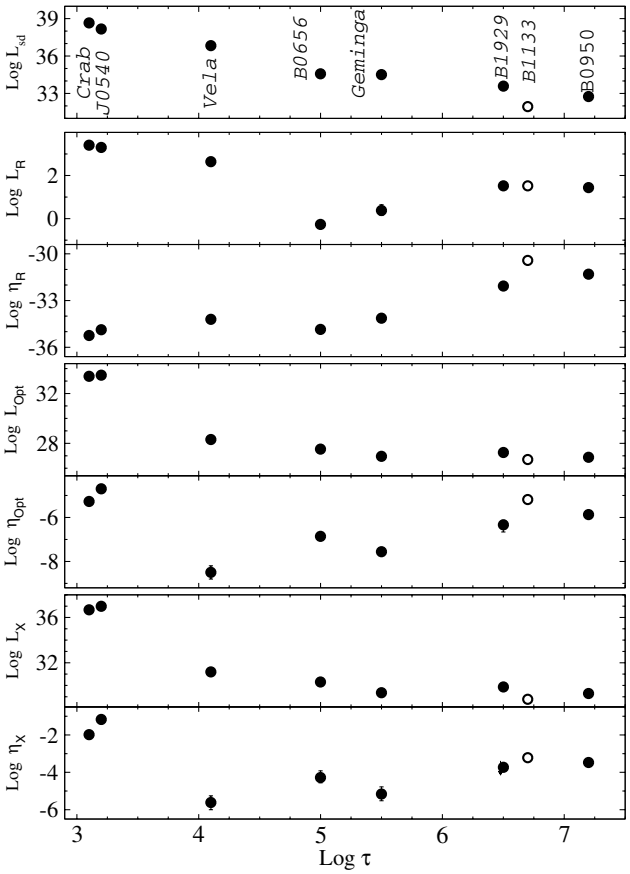

Fig. 5. The evolution of the pulsar radio, optical and X-ray luminosities, and respective efficiencies with the characteristic age τ. The *top panel* shows corresponding spin-down luminosities.

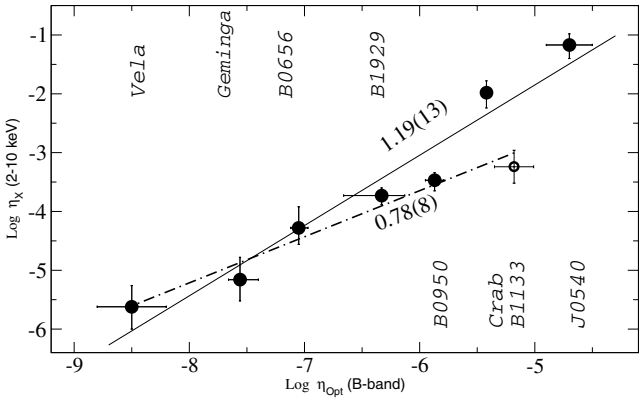

Fig. 6. Relations between the optical $\eta_{\rm Opt}$ and X-ray $\eta_{\rm X}$ efficiencies in the B-band and 2–10 keV ranges. Solid line shows the best linear regression fit for a sample of pulsars from Zharikov et al. (2006). The dot-dashed line is the similar fit only for the set of the pulsars that includes PSR B1133+16 counterpart candidate and excludes the youngest Crab and PSR J0540-69. Numbers are the line slopes with their errors in brackets.

does not invalidate the previous conclusion regarding the high optical and X-ray efficiencies of old pulsars, which become comparable to those of the young Crab-like pulsars. At the same time, its position on the $\eta_{\rm Opt}$–$\eta_{\rm X}$ plane significantly deviates from the previous relation (Fig. 6). Two of its neighbors, PSR B1929+10 and PSR B0950+08, also show apparent deviations. However, if we exclude from the sample the two youngest pulsars, the Crab pulsar and PSR B0540-69, we obtain a new relation that fits the rest pulsars nicely, including the PSR B1133+16 candidate. This is not a surprise, since noticed Zharikov et al. (2004) that the young pulsars are distinct from the older ones by their X-ray and optical efficiencies and displacement on the $\eta_{\rm Opt}$–$\dot{E}$ and $\eta_{\rm X}$–$\dot{E}$ planes. Therefore, in both respects the proposed candidate is not outstanding. That can be considered as additional evidence that it is the real counterpart of PSR B1133+16.

Despite the high transverse velocity of PSR B1133+16, we did not detect any developed Balmer bow shock nebula of the pulsar. This suggests low ISM density in the pulsar neighborhood that is compatible with its high galactic latitude $\approx$69°, low $E(B-V)=0.04$ towards the pulsar, and a small hydrogen column density $N_{\rm H}=(1\text{–}2)\times10^{20}$ cm^{-2} (Kargaltsev et al. 2006) estimated from the measured pulsar dispersion measure of 4.86 cm^{-3} pc and the spectral fit of the candidate X-ray counterpart. Nevertheless, the emission detected at about the 3σ detection limit in the pulsar position error ellipse in the H$_\alpha$ image (object C) may come out from the brightest part of the bow shock head and/or from a clump of the ISM with a higher density. The low S/N ratio does not allow us to conclude this confidently. The absence of object C in our B and R broad band images prabably excludes its background origin. Accounting for deep B and R magnitude upper limits and a high galactic latitude with low $E(B-V)$, object C certainly cannot be a star from our Galaxy. Any background extragalactic object is also very unlikely since it would be detected first of all in our deep broad band images.

Instead of the bow shock, we note two marginal but likely spatially correlated extended features in the H$_\alpha$ emission and X-rays, which are reminiscent of a "tail" behind the pulsar. If the X-ray and the H$_\alpha$ tails are indeed associated with the pulsar, this would present the first example of when the pulsar tail is detected simultaneously in the H$_\alpha$ and X-rays. The combinations of the X-ray tails and H$_\alpha$ bow shocks for a few pulsars have been reported in the literature (see, e.g., Zavlin 2006, for a short review). Most recently such a tail has been reliably detected in X-rays with the XMM behind PSR B1929+10 (Becker et al. 2006), which is also a member of the sample considered above. However, despite these efforts, no counterparts of the tails have been detected so far in the optical range to our knowledge. The formation of the H$_\alpha$ tails does not look unreasonable when a compressed pulsar wind behind a supersonically moving NS cools via X-ray emission that ionizes the ambient matter on larger spatial scales, which then recombines producing H$_\alpha$ photons. An apparent offset of the X-ray tail candidate from the H$_\alpha$ elongated structure in our case (cf. the images with contours in the H$_\alpha$ – R and X-ray panels in Fig. 4) is consistent with such a scenario.

The suggested candidate optical and X-ray counterparts of PSR B1133+16 and its tail can be easily verified by a followup imaging of the field in the optical and X-rays on the basis of a few years. Given the pulsar proper motion, the candidates, if they are the real counterparts, will be shifted from the detected positions roughly to the north by about 1.″4–1.″8 by the end of 2008. Such a shift can be reliably measured using the subarcsecond spatial resolutions of 8 m-class optical telescopes and the Chandra X-ray observatory.

Acknowledgements. We are grateful to the anonymous referee for many useful comments and suggestion that allowed us to improve this paper considerably. This work has been partially supported by CONACYT 48493 and PAPIIT IN101506 projects, RFBR (grants 05-02-16245 and 05-02-22003), FASI (grant NSh-9879.2006.2), and Fondecyt 1070705. We used the USNOFS Image and Catalogue Archive operated by the United States Naval Observatory, Flagstaff

Station (http://www.nofs.navy.mil/data/fchpix/). This work is based on observations made with the European Southern Observatory telescopes obtained from the ESO/ST-ECF Science Archive Facility. The Munich Image Data Analysis System is developed and maintained by the European Southern Observatory.

References

Becker, W., Kramer, M., & Jessner, A. 2006, ApJ, 245, 1421
Bhat, N. D., Gupta, Y., Kramer, M., et al. 2007, A&A, 462, 257
Brisken, W. F., Benson, J. M., Goss, W. M., et al. 2002, ApJ, 571, 906
Gaensler, B. M., & Slane, P. O. 2006, ARA&A, 44, 17
Gallant Y., et al. 2000, ESO/VLT program 66.D-0069(A)
Cordes, J. M., Romani, R. W., & Lundgren, S. C. 1993, Nature, 362, 133
Kargaltsev, O., Pavlov, G. G., & Romani, R. 2004, ApJ, 602, 327
Kargaltsev, O., Pavlov, G. G., & Garmire, G. P. 2006, ApJ, 636, 406
Landolt, A. 1992, AJ, 104, 340
Mignani, R. 2005, Proc. NATO/ASI Conf.: The Electromagnetic Spectrum of Neutron Stars, Held in Maramaris, Turkey, June 7–18, 2004 [arXiv:astro-ph/0502160]
Mignani, R., & Caraveo, P. 2001, A&A, 376, 213
Mignani, R., De Luca, A., Caraveo, P., & Becker, W. 2002, ApJ, 580, L143
Mignani, R., Manchester, R. N., & Pavlov, G. G. 2003, ApJ, 582, 978
Newberry, M. V. 1991, PASP, 103, 122
Fukugita, M., Shimasaku, K., & Ichikawa, T. 1995, PASP, 107, 945
Pavlov, G. G., Stringfellow, G. S., & Cordova, F. A. 1996, ApJ, 467, 370
Percival, J. W., Bigg, J. D., Dolan, J. F., et al. 1993, ApJ, 407, 276
Schlegel, D., Finkbeiner, D., & Davis, M. 1998, ApJ, 500, 525
Shibanov, Yu., Zharikov, S., & Komarova, V. 2006 A&A, 448, 313
Zavlin, V. E., & Pavlov, G. G. 2004, ApJ, 616, 452
Zavlin, V. E. 2006, Proc. Isolated Neutron Stars: from the Interior to the Surface, April 24–28, 2006 – ed. D. Page, R. Turolla, & S. Zane, ASpS, in press [arXiv:astro-ph/0608210]
Zharikov, S., Shibanov, Yu., Koptsevich, A., et al. 2002, A&A, 394, 633
Zharikov, S., Shibanov, Yu., Mennickent R., et al. 2004, A&A, 417, 1017
Zharikov, S., Shibanov, Yu., & Komarova, V. 2006, AdSpR, 37, 1979